PAPER

Check for updates

Effect of the organic sulfur source on the photocatalytic activity of CdS†

Qiong Zhu,[a] Jinhua Wang,[a] Si Chen,[a] Hongquan Fu,[a] Juan Zhang,[a] Hejun Gao [ID] *[ab] and Yunwen Liao*[a]

By controlling the species of the organic sulfur source, CdS samples were produced with different photocatalytic performances by a low-temperature solvothermal method. Different species of the organic sulfur source were chosen as the coordination agent to control the interactions in the crystal growth process. Among them, thioacetamide was the best coordination agent. The hydrophobic chain could be good for reducing the resistance of charge transfer, and increasing the rate of surface charge transfer and the lifetime of the photoexcited electrons. Benefiting from the hydrophobic chain, CdS shows an excellent photocatalytic hydrogen evolution rate of 943.54 μmol h^{-1} g^{-1} and a rhodamine B photocatalytic degradation rate of 99.1% in 60 min, which is superior to the photocatalysis of pure CdS prepared by many other methods.

1 Introduction

With the development of society and industrial progress, serious problems, such as energy shortage and environmental pollution, have become the major problems besetting mankind.[1] The green technology of photocatalysis provides an essential pathway for solving the problems of energy shortage and environmental pollution.[2] Semiconductor photocatalysts have a good photocatalytic activity for reducing the water to hydrogen (H$_2$).[3,4] Photocatalytic semiconductors could effectively convert organic pollutants to inorganic compounds, such as carbon dioxide and water, too.[5,6] The existing amount of photocatalytic semiconductors is numerous and the performance of a photocatalyst varies greatly with the preparation method.[7,8] Therefore, it is important to explore the influence regularity of the preparation of photocatalysts with excellent photocatalytic activity.

In recent years, CdS, as a non-precious metal photocatalyst, has received extensive attention due to its suitable bandgap (∼2.4 eV), absorption of visible light, band-edge position for photocatalytic hydrogen degradation and hydrogen evolution.[9,10] However, the rapid recombination rate of hotpogenerated electrons and holes and low electric conductivity and many defects are present in the current preparation of CdS.[11–13] It leads to an unstable photocatalytic performance in practical application. In order to overcome these shortcomings, many strategies have been proposed, such as element doping (Ni, Co, and P),[14–16] construction of heterogeneous structures (CuO, CeO$_2$, and ZnO),[17–21] *etc.* Shangguan *et al.*[22] reported that the Bi-metal-doped CdS photocatalyst has a higher photocatalytic efficiency, which could be ascribed to the enhanced light absorption ability and charge separation after Ni and Mo were introduced. Lu *et al.*[23] reported a novel 0D/1D direct Z-scheme heterojunction photocatalyst synthesized by *in situ* anchoring W$_{18}$O$_{49}$ QDs onto the surface of CdS NRs. Both bulk photogenerated carriers and surface photogenerated carriers are separated efficiently, achieving a dramatically improved photocatalytic H$_2$ evolution performance. Xu *et al.*[24] reported that superoxide radicals and holes worked together for the ciprofloxacin degradation by the direct Z-scheme Bi$_3$TaO$_7$–CdS semiconductor materials. Although element doping and constructing heterojunction could enhance the photocatalytic activity of CdS, the preparation of these complex photocatalysts is complex and the photocatalytic efficiency of the photocatalyst is also difficult to maintain. Therefore, the study of pure CdS in photocatalytic systems cannot be ignored. However, pure CdS often has very low photocatalytic performance, so it will be of great use to optimize its performance. F. Vaquero *et al.*[25] prepared pure CdS with different morphologies by changing the thermal solvent, and the highest hydrogen production performance reached 502 μmol g^{-1} h^{-1}. At the same time, they also adjusted the crystallinity of pure CdS by changing the reaction temperature. The hydrogen production performance of CdS with high crystallinity was significantly improved, up to 500 μmol g^{-1} h^{-1}.[26] Bie *et al.*[8] improved the photocatalytic activity of CdS by adjusting the thickness, up to 2155 μmol g^{-1} h^{-1}. Therefore, it is significant

[a] College of Chemistry and Chemical Engineering, Chemical Synthesis and Pollution Control Key Laboratory of Sichuan Province, China West Normal University, Nanchong, Sichuan 637000, China. E-mail: hejun_gao@126.com; liao-yw@163.com

[b] Institute of Applied Chemistry, China West Normal University, Nanchong 637000, China

to improve the photocatalytic activity of pure CdS and optimize its preparation process.

Types of sulfur source of CdS are numerous. It includes organic and inorganic compounds. For inorganic sulfur sources, Sun et al.[27] reported that CdS hollow microspheres could be prepared by a photochemical preparation technology using $Na_2S_2O_3$ as a sulphur source. Maimaiti et al.[28] prepared CdS by the precipitation reaction using a sulphur source of Na_2S. Organic sulfur sources are more applied in CdS preparation than inorganic sulfur sources. Navarro et al.[25] reported that CdS crystals with different morphologies could be obtained using thiourea a sulphur source. Li et al.[29] reported that the umbrella-like CdS with exposed high-activity (002) facets was successfully synthesized by using NH_4SCN as the sulfur source. The unprecedented (110)-bound CdS rhombic dodecahedra were produced by using thioacetamide as the sulfur source.[30] However, the effect of organic sulfur on the CdS for the photocatalytic performance has scarcely been reported.

In this work, thioacetamide (CH_3CSNH_2), thiourea (NH_2-$CSNH_2$), and thiosemicarbazide ($NH_2CSNHNH_2$) have been used to investigate the effect of the structure of organic sulfur on the CdS. This work focuses on the structure, photoelectric properties, and catalytic properties of CdS, which are changed with the increase of the hydrophobicity of organic sulfur sources. This work will promote the development of CdS material, especially in the regulation of sulfur source, band structure, and morphology design.

2   Experimental section

2.1   Materials

Cadmium acetate ($Cd(CH_3COO)_2 \cdot 2H_2O$, AR), sodium sulfide ($Na_2S$, AR), and thioacetamide (CH_3CSNH_2, AR) were obtained from Aladdin Co. Ltd (Shanghai, China). Thiourea (NH_2CSNH_2, AR) and thiosemicarbazide ($NH_2CSNHNH_2$, AR) were purchased from Adamas Reagent, Ltd (Shanghai, China). Triethylenetetramine ($C_6H_{18}N_4$, AR) was provided by Xiya Reagent Co. Ltd (Shangdong, China). Anhydrous ethanol (C_2H_5OH, AR), rhodamine B ($C_{28}H_{31}ClN_2O_3$, AR) and lactic acid ($C_3H_6O_3$, AR) were purchased from Kelong Chemical Reagent Co. Ltd (Chengdu, China). All chemicals were used directly without further purification. Ultra-pure water was used for all experiments. All the data were measured in triplicate.

2.2   Synthesis of CdS

CdS photocatalyst was prepared by a one-step solvothermal method. In general, 2 mmol cadmium acetate and 10 mmol sodium sulfide were dissolved in 60 mL triethylenetetramine and ethanol mixed solvent (2 : 1 by volume). After stirring for 1 hour, the solution was transferred to a 100 mL Teflon stainless steel autoclave and kept at 80 °C for 48 h. The precipitate was collected by centrifugation and washed several times with ultra-pure water and ethanol. The samples were then freeze-dried for 72 h, which were denoted as S-NS. Sodium sulfide was replaced by CH_3CSNH_2, NH_2CSNH_2 and $NH_2CSNHNH_2$ (Fig. 1), which were denoted as S-TAA, S-TA, and S-TSC, respectively.
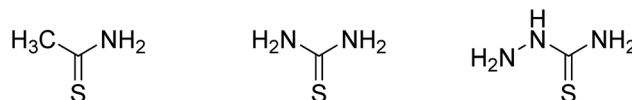

Fig. 1   Structure of thioacetamide, thiourea, and thiosemicarbazide.

2.3   Characterization

The crystal structure of the sample was studied using an X-ray diffractometer (XRD, Ultima IV, Rigaku Ltd., Japan) with Cu-Kα radiation ($\lambda = 0.15418$ nm). Ultraviolet-visible diffuse reflectance spectroscopy (DRS) was performed using an ultraviolet-visible spectrophotometer (Shimadzu UV-2600, Japan), with $BaSO_4$ as the substrate, and the wavelength was between 200 and 800 nm. A field emission scanning electron microscope (FE-SEM, ZEISS Gemini-SEM 500, Germany) was used to explore the morphology of the sample. High-resolution transmission electron microscope (HR-TEM) images were obtained (FEI Quanta 250 FEG electron microscope, USA) with an acceleration voltage of 200 kV. A fluorescence spectrometer (G9800A, Japan) was used to obtain photoluminescence (PL) emission spectra of the samples, which were excited at 310 nm.

2.4   Photocatalytic H_2 production

Photocatalytic hydrogen testing was carried out in a Labsolar-6a all-glass automatic on-line trace gas analysis system (Beijing PerfectLight Co., Ltd., China). A 300 W xenon lamp (PLS-SCE300D, Beijing PerfectLight Co., Ltd.) with a UV cut-off filter ($\lambda \geq 420$ nm) was used as the visible light source in the photoreaction system. 50 mg sample was added to 100 mL solution (8% lactic acid) for 4 h at 6 °C. Gas chromatography (GC7900, Tianmei Scientific Instrument Co., Ltd., China) was used to detect the content of H_2 in the system by automatic interval sampling.

The apparent quantum efficiency (AQE) was measured using a PLS-SXE300D with a 420 nm ($\pm$5 nm) band pass filter (irradiation conditions 52 W m^{-2}). AQE was obtained by eqn (1):[31]

$$\begin{aligned} AQE\ (\%) &= \frac{\text{number of reacted electrons}}{\text{number of incident photons}} \times 100 \\ &= \frac{\text{number of evolved } H_2 \text{ molecules} \times 2}{\text{number of incident photons}} \times 100 \end{aligned} \tag{1}$$

2.5   Photocatalytic degradation

Rhodamine B was degraded under visible light to evaluate the photocatalytic activity of CdS. The general process was as follows: 20 mg sample was dispersed in 50 mL of 10 mg L^{-1} rhodamine B solution. After reaching the adsorption–desorption equilibrium, 4 mL of uniform suspension was collected. Subsequently, the remaining suspension system was illuminated with PLS-SXE300D ($\lambda \geq 420$ nm), and samples were taken at intervals of 10 minutes, and the photocatalytic reaction was ended after 60 min. The collected sample was centrifuged at 8000 rpm for 5 min, and the supernatant was retained. The concentration of residual rhodamine B in the supernatant was

measured with an ultraviolet-visible spectrophotometer at a wavelength of 554 nm.

2.6 Photoelectrochemical measurements

The transient photocurrent response was recorded using an electrochemical workstation (CHI660E, CH Instruments Co., China). Ag/AgCl was used as the counter electrode and Pt was the reference electrode. The working electrode was prepared by coating the sample on a piece of FTO glass of 1 cm^2. PLS-SXE300D was used as the light source and 0.5 M Na_2SO_4 solution was used as the electrolyte. The samples were characterized by open-circuit photovoltage (OCPV) and electrochemical impedance spectroscopy (EIS) in the same environment.

3 Results and discussion

The morphologies of the S-NS, S-TAA, S-TA, and S-TSC were investigated using FE-SEM and HR-TEM. Fig. 2 shows the FE-SEM images of the samples with very different morphologies. As shown in Fig. 2a and b, the S-NS sample exhibits non-uniform micron-sized bulk solid, which was formed by agglomeration of small nanoparticles. When the inorganic sulfide source NaS was substituted with an organic sulfide source CH_3CSNH_2, the morphologies changed a lot (Fig. 2c and d). It revealed highly uniform and homogeneous micron particles with diameters of about 1 μm. It was composed of several nanoparticles. When $-CH_3$ in CH_3CSNH_2 was replaced by $-NH_2$ (NH_2CSNH_2), the morphology of CdS was changed again, as shown in Fig. 2e and f. Some microspheres were gradually formed and a surface with netlike and porous structures was produced on the surface of S-TA. When one $-NH_2$ group in NH_2CSNH_2 was replaced by $-NH_2NH_2$ ($NH_2NH_2CSNH_2$), a three-dimensional porous structure and network was obtained (Fig. 2g and h). It showed that the S-TSC formed hollow and fluffy microspheres. With the increase of the hydrophilicity of the organic sulfur source, the morphology of the CdS changed from a solid aggregation state to a 3D fluffy network structure. The hydrophobicity or hydrophilicity of the organic sulfur source has a great influence on the morphology of the CdS, which will affect the photocatalytic performance of CdS.

The results of HR-TEM were consistent with the SEM results. S-TAA was composed of several nanoparticles (Fig. 3a). The (111) facet preference of S-TAA can be demonstrated by HR-TEM images. Fig. 3b showed that the only visible crystal plane space in S-TAA was 0.336 nm, which was attributed to the (111) facet in cubic CdS.[32] The clear lattice fringes could not be observed in some areas (dash part in Fig. 3b). It could be due to the low solvothermal temperature (80 °C), which was unable to produce sufficient energy to form high crystallinity. The (200) and (311) facets may be only in the initial state.

XRD analysis was performed to investigate the crystalline structure of the CdS samples (Fig. 4a). The absence of any impurities was evident from the powder X-ray diffractograms, indicating that the pure CdS photocatalyst can be prepared from various sulfur sources. The diffraction peaks at 26.56°, 43.92° and 52.11° were attributed to the lattice planes of (111),
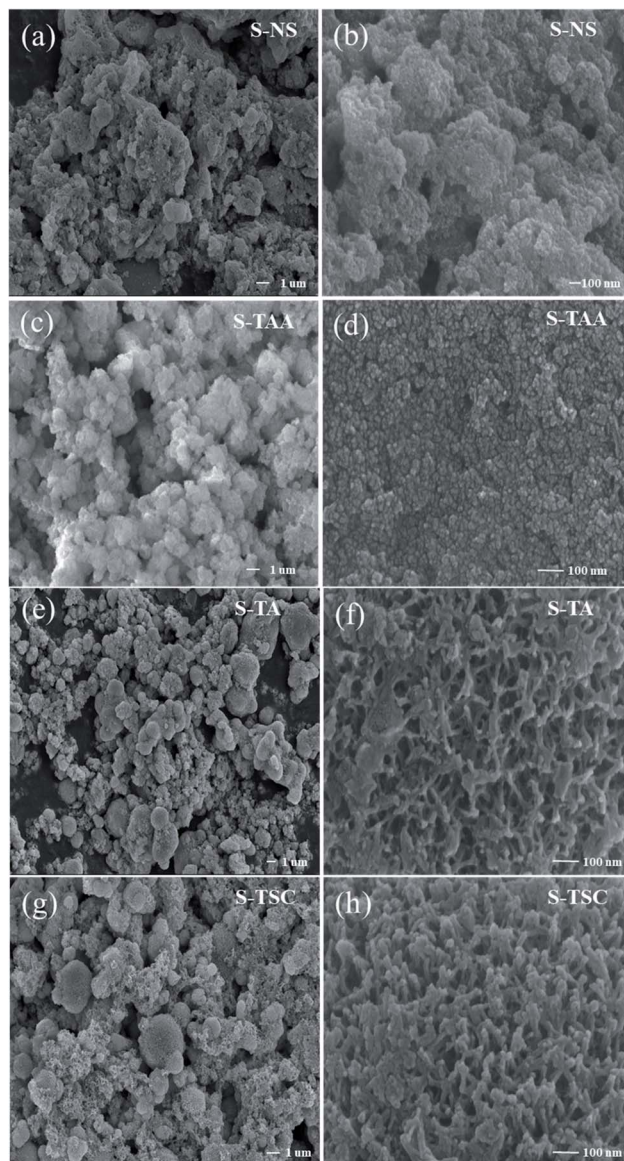

Fig. 2 FE-SEM images of S-NS (a and b), S-TAA (c and d), S-TA (e and f), and S-TSC (g and h).
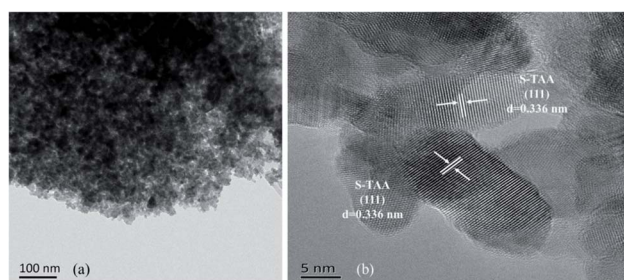

Fig. 3 TEM and HRTEM images of S-TAA (a and b).

(220) and (311) of cubic CdS, respectively (JSPDS card no. 42-1411, $a = 5.818$ Å).[33] It is not difficult to find that the diffraction peaks corresponding to those (111) crystal facets of S-NS, S-TSC
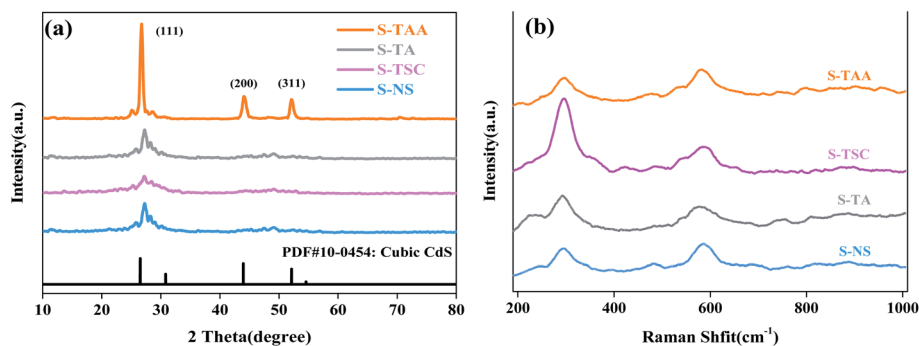
Fig. 4 XRD patterns (a) and Raman spectra of different samples (b).

and S-TA are flat and low wide peaks. The diffraction peaks of (200) and (311) crystal facets can hardly be observed. This could be due to the low crystallinity degree of the samples. However, S-TAA shows sharp peaks with high diffraction intensity, which is due to the high crystallization of S-TAA in the preparation process. It shows that the low crystalline CdS photocatalyst was obtained using Na_2S, NH_2CSNH_2 and $NH_2CSNHNH_2$ as a sulfur source at low temperature. The sulfur source of CH_3CSNH_2 is favorable for the prepared highly crystalline cubic CdS. The reason could be that the hydrophobic groups ($-CH_3$) were more conducive to adsorption on the surface of the crystal nucleus than the hydrophilic groups ($-NH_2$). According to the layer growth theory, the crystal nucleus may gradually grow and accumulate into compact cubic CdS.

The crystallite size of the four samples was obtained by Debye–Scherrer's formula,[34]

$$D = \frac{k\lambda}{\beta \cos \theta} \quad (2)$$

where D is the crystallite size, k is 0.94, λ is the wavelength of the X-ray radiation (1.5 Å), β is the full width half maximum and θ is the angle of diffraction. The average particle size was 3.2, 17.1, 1.6 and 2.7 nm for S-NS, S-TAA, S-TA, and S-TSC, respectively. It indicated that the hydrophobic groups ($-CH_3$) led to a further increase in the crystallite sizes.

Raman spectra measurements were carried out to characterize the chemical structure of CdS. Fig. 4b displays the Raman spectra of pure CdS using various sulfur sources. Two peaks at 296 and 585 cm^{-1} correspond to first-order 1 LO and second-order 2 LO phonon scattering of cubic CdS, respectively.[35,36] 1 LO is reported to appear around 300 cm^{-1} in micron and nanometer-sized particles, and is the prominent peak in all the reported results on CdS samples, while the value obtained in the present study is around 293 cm^{-1}. This frequency shift of the 1 LO Raman peak in CdS is mainly ascribed to the grain size effect. Due to the grain size effect, the value of 1 LO had red-shifted by 4 cm^{-1} (297 cm^{-1}).

The specific surface area and pore size distributions of cubic CdS were obtained by nitrogen adsorption–desorption isotherms (Fig. 5). It showed that all CdS samples exhibit a type IV isotherm and H3 hysteresis loop,[37] which implies the formation of porous structures in the cubic CdS.[38,39] The BET specific surface areas of cubic CdS, which were obtained using Na_2S, CH_3CSNH_2, NH_2CSNH_2 and $NH_2CSNHNH_2$ as a sulfur source, were calculated to be 164.2, 99.3, 151.3, and 301.1 m^2 g^{-1}, respectively. The more the availability of hydrophilic groups in organic sulfur sources, the larger the specific surface area. The average pore size distribution of the S-TA and S-TSC mainly centered at 3–4 nm. This indicated that the hydrophilic groups were good for the construction of a narrow pore size distribution. S-TAA exhibited wide pore size distribution (>5 nm), implying that S-TAA was a mesoporous material.

The UV-vis DRS spectrum was recorded for cubic CdS in the range between 400 nm and 800 nm,[40] which were obtained using NaS, CH_3CSNH_2, NH_2CSNH_2 and $NH_2CSNHNH_2$ as a sulfur source (Fig. 6). The corresponding absorption band
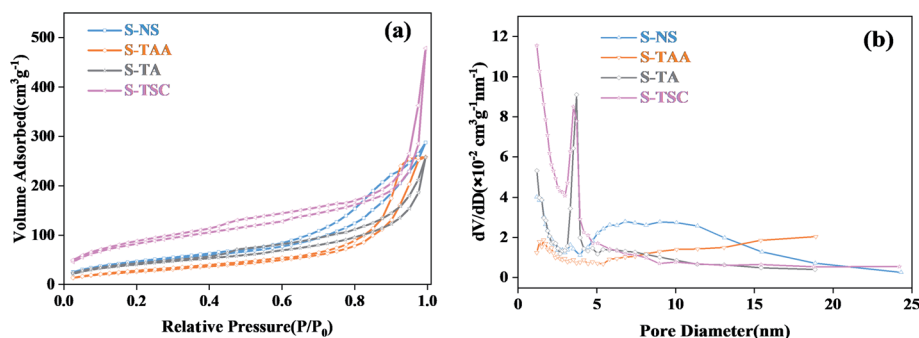

Fig. 5 The N_2 adsorption–desorption isotherm of the prepared samples (a) and corresponding pore size distributions (b).
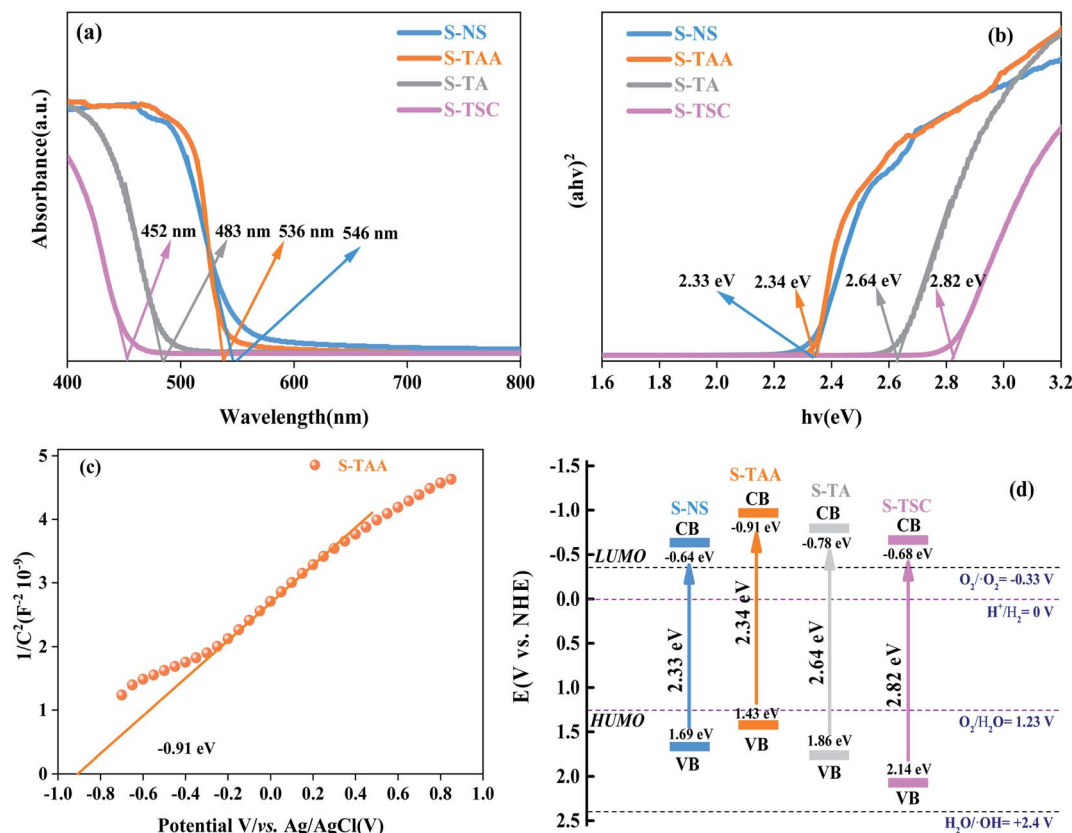
Fig. 6 UV–vis DRS spectra of the different materials (a), Kubelka–Munk plots of the different materials (b), Mott–Schottky plot of S-TAA (c) and band structure alignments of the different materials (d).

edges of S-NS, S-TAA, S-TA and S-TSC are 546 nm, 536 nm, 483 nm and 452 nm respectively. With the increase in the hydrophobicity of the sulfur source, the photoabsorption edge of CdS moved to the visible region gradually (Fig. 6a).

The band gap energy of CdS could be calculated by[41]

$$\alpha h\nu = A(h\nu - E_g)^{n/2} \qquad (3)$$

where α, h, ν, A, and E_g are the absorption index, Planck constant, frequency, constant value, and band-gap energy of the semiconductor, respectively. The material type is a direct semiconductor ($n = 1$) or indirect semiconductor ($n = 4$), and n for CdS is 1. The band gap energies were 2.33, 2.34, 2.64, and 2.82 eV for S-NS, S-TAA, S-TA, and S-TSC, respectively (Fig. 6b). The increase in the hydrophobicity of the sulfur source caused a significant change in the band gap energy. In other words, this hydrophobicity of the sulfur source would be conducive to decreasing the band gap energy of cubic CdS. Mott–Schottky analysis was used to investigate the effect of hydrophobicity on the conduction band (CB) and the valence band (VB) of cubic CdS. The slope of the Mott–Schottky plots of all the samples was positive (Fig. 6c and S1†), indicating that they are n-type semiconductors. The flat-band potentials (E_{fb}) of S-NS, S-TAA, S-TA and S-TSC are −0.64, −0.91, −0.78 and −0.68 eV, respectively. For n-type semiconductors, the E_{CB} is more negative by about −0.2 V than the flat band potential.[42] Therefore, the E_{CB} for S-

NS, S-TAA, S-TA and S-TSC was about −0.64, −0.91, −0.78 and −0.68 eV *versus* the normal hydrogen electrode (NHE) ($E_{NHE} = E_{Ag/AgCl} + 0.197$ eV).[43] With the increase in the hydrophobicity of the sulfur source, the conduction bands of CdS become more and more negative, which indicates that the proton reduction ability becomes stronger and stronger. It is conducive to the production of H2.

PL spectra can show the photoelectron–hole pair recombination in semiconductors. The lower PL intensity corresponds to the lower photoelectron–hole pair recombination efficiency.[31,44] As shown in Fig. 7a, the PL strength of S-TAA is lower than that of S-NS, S-TA and S-TSC, indicating that the recombination rate of lower photoelectron–hole pairs could be inhibited effectively by increasing the hydrophobicity of the sulfur source.

The separation and migration rates of photocarriers were further studied by I–t and EIS measurements. As shown in Fig. 7b, S-TAA exhibited the highest photocurrent response in all samples, indicating that the increase of the hydrophobicity of the sulfur source was beneficial to enhance the separation rate of the photocarriers. The Nyquist plot is shown in Fig. 7c. The S-TAA exhibited a minimum radius of curvature, indicating that the increase of the hydrophobicity of the sulfur source favors reducing the resistance of charge transfer and increasing the rate of surface charge transfer.[45]
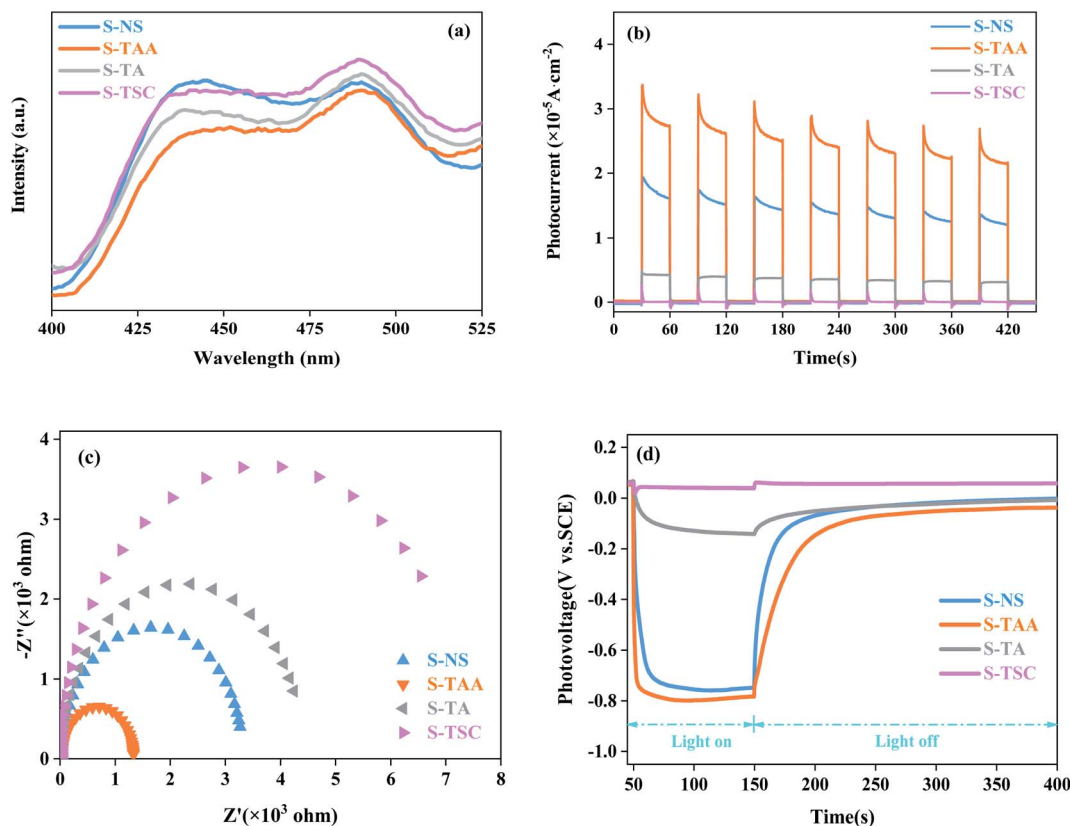
Fig. 7 PL spectra of different materials (a), transient photocurrent response of different materials (b), EIS Nyquist plot (c) and OPCV spectrum (d).

OPCV can be used to evaluate the lifetime and separation efficiency of photocarriers.[46,47] Fig. 7d shows the OPCV of samples. S-TAA had the largest open-circuit photovoltage response, indicating that the photoexcited electrons had a long lifetime in the S-TAA sample.[48] It showed that the increased photocatalysis activity of CdS was caused by increasing the lifetime of the photoexcited electrons through the elevated hydrophobicity of the sulfur source.

The hydrogen-evolving activity of samples was evaluated under visible light ($\lambda \geq 420$ nm) using 10% lactic acid as the sacrificial agent. After four hours, the order of hydrogen evolution was as follows: S-TAA > S-TA > S-TSC > S-NS (Fig. S2†).

The hydrogen evolution of S-NS was the lowest in all samples (only 49.2 μmol) after four hours of illumination. It indicated that the improvement of CdS photocatalytic efficiency by the organic sulfur source is better than that by the inorganic sulfur source. Obviously, S-TAA has a larger hydrogen evolution rate than other samples and the quantum efficiency was about 10.58%. The rate of hydrogen evolution of S-TAA was 1.7, 2.0 and 3.8 times that of S-TA, S-TSC and S-NS, respectively (Fig. 8a). The hydrogen production rate of S-TAA reached 943.54 μmol g^{-1} h^{-1}, which is higher than that of CdS prepared by many other methods (Table 1). It implied that the increase of hydrophobicity of the sulfur source could greatly enhance the
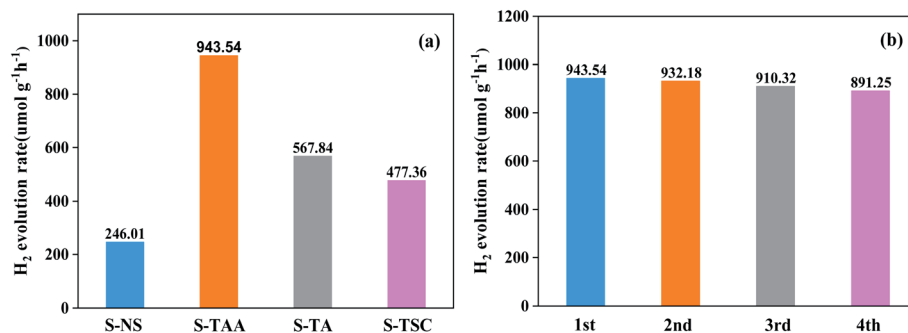

Fig. 8 The photocatalytic hydrogen evolution performance for all samples (a) and repeated photocatalytic hydrogen evolution experiments of S-TAA (b).
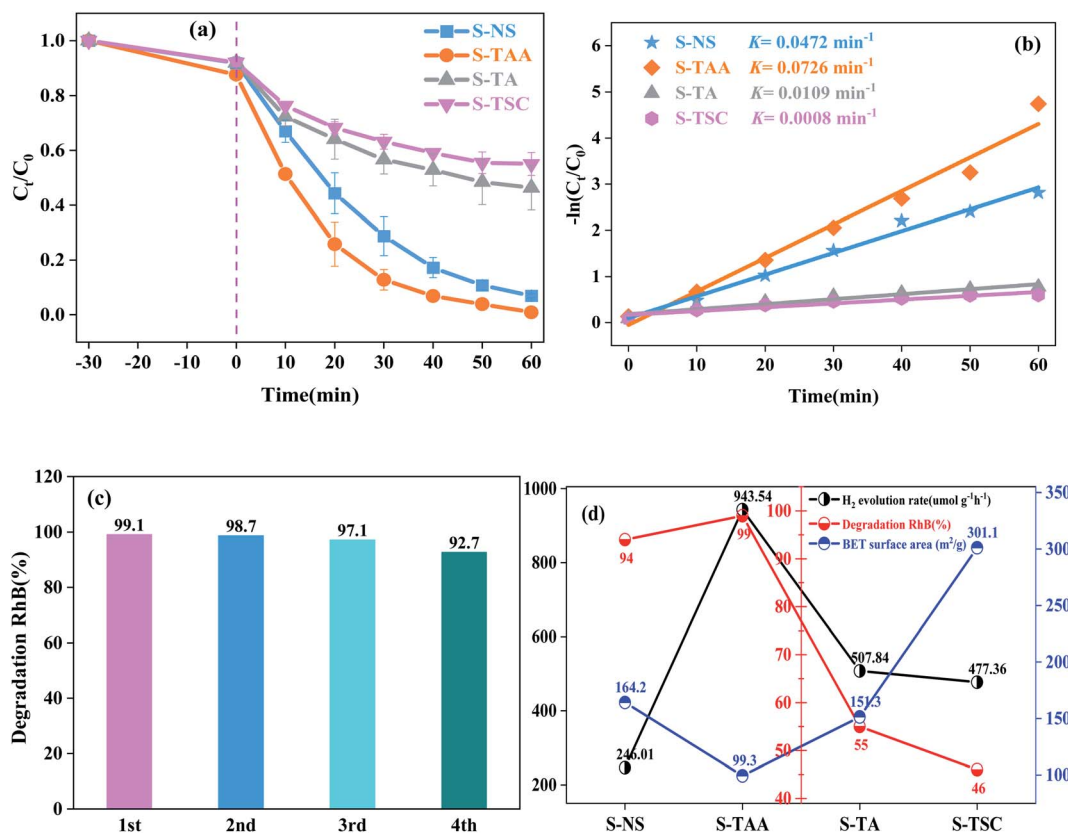
Table 1 Comparison of H_2 evolution rate and the apparent quantum efficiency AQE of different photocatalytic H_2 production systems[a]

Entry	Cat.	Sacrificial reagent	H_2 yield ($\mu mol\ g^{-1}\ h^{-1}$)	AQE (%)
This work	S-TAA	Lactic acid	943.54	10.58
1 (ref. 25)	CdS-EDA	$Na_2S–Na_2SO_3$	502	NA[1]
2 (ref. 26)	CdS-120	$Na_2S–Na_2SO_3$	500	NA[1]
3 (ref. 8)	5-CdS	$Na_2S–Na_2SO_3$	2155	7.8
4 (ref. 49)	NiS/CdS-T200	Lactic acid	542	NA[1]
5 (ref. 50)	MoO_xS_y/CdS	Methanol	460.43	NA[1]
6 (ref. 51)	CdS/rGO	$Na_2S–Na_2SO_3$	500	NA[1]
7 (ref. 52)	CuO/WO_3/CdS	MB	44.5	NA[1]

[a] For better comparison, data were converted to $\mu mol\ g^{-1}\ h^{-1}$.

Table 2 Comparison of RhB photocatalytic degradation performance of different catalysts

Entry	Cat.	Conc. ($mg\ L^{-1}$)	Dosage (mg)	t (min)	De. (%)
This work	S-TAA	10	20	60	99
1 (ref. 53)	MgCdS	10	50	70	96
2 (ref. 54)	Cd/CdS/BiOCl	10	10	150	90
3 (ref. 55)	CdS/BiOCl	10	50	100	90
4 (ref. 56)	CdS/AgBr-rGO	24	60	60	96
5 (ref. 57)	BiOI/CdS	20	20	60	94
6 (ref. 58)	CdS/$BiVO_4$	15	10	60	95
7 (ref. 59)	Tetrapod CdS	60	30	140	99

Fig. 9 Photocatalytic degradation curve of RhB by photocatalytic materials under visible light (a), degradation kinetic curve of RhB by different photocatalytic materials (b), repeated degradation experiments of S-TAA for photocatalytic degradation of RhB (c), and H_2 evolution rates, RhB degradation and BET surface area obtained on the prepared CdS samples (d).
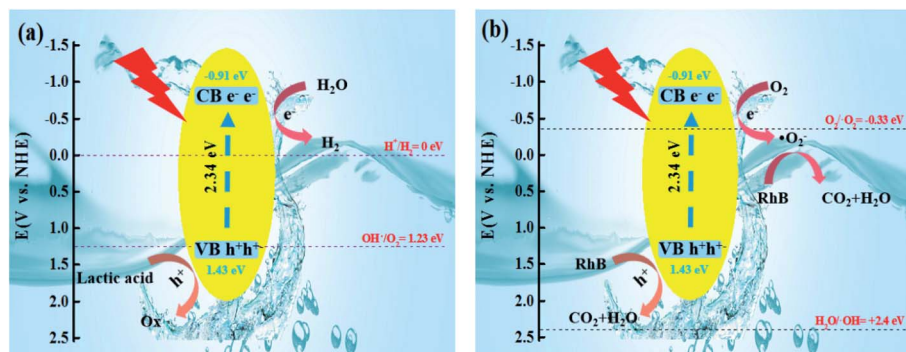
Fig. 10 Graphical illustration of the mechanism for the photocatalytic degradation-hydrogen evolution of RhB over the S–TAA photocatalyst (a and b).

photocatalytic activity of H_2 evolution of CdS. After four cycles, the hydrogen evolution rate of S-TAA remained at about 900 $\mu mol\ h^{-1}\ g^{-1}$, and the hydrogen evolution rate decreased less than 6% (Fig. 8b). This indicates that S-TAA has a good photocatalytic stability.

The photocatalytic degradation properties of samples were evaluated under visible light irradiation ($\lambda \geq 420$ nm) with RhB as the target pollutant. The degradation curves of RhB by S-TAA, S-TA, S-TSC and S-NS accord with the first-order-kinetic equation:[34]

$$\ln(C_0/C_t) = kt \qquad (4)$$

where t and k are the visible light irradiation time and degradation rate constant, respectively. Compared with CdS prepared by many other methods, S-TAA shows superior photocatalytic degradation performance. Within 60 min, the degradation efficiency of RHB is close to 99.1%, which is better than many CdS based composites (Table 2). The order of photocatalytic degradation activity is as follows: S-TAA > S-NS > S-TA > S-TSC (Fig. 9a). The photocatalytic degradation rates of S-TAA were 1.5, 6.7 and 90.8 times higher than those of S-NS, S-TA and S-TSC, respectively (Fig. 9b). This shows that the increase of hydrophobicity of the organic sulfur source improves the photocatalytic degradation performance. After four cycles, the degradation rate of S-TAA remained at about 93% and the degradation rate decreased less than 6.5% (Fig. 9c). It also implies that S-TAA has good photocatalytic stability.

The stronger hydrophobicity of organic sulfur source are available, the smaller the specific surface area it is (Fig. 9d). However, the photocatalytic activity of S-TAA was better than that of the other samples. Therefore, the influence of specific surface area on photocatalytic activity was not dominant in this work, and the hydrophobicity of the organic sulfur source played an important role in CdS photocatalytic activity.

Due to the increase in the hydrophobicity of the sulfur source, the structure of CdS had been changed. The CB of S-TAA was more negative than that of S-NS, S-TA, and S-TSC. The VB of S-TAA was more positive than that of S-NS, S-TA, and S-TSC. In the photocatalytic hydrogen evolution, H_2O was reduced by

electrons to produce hydrogen, hydroxyl radicals were oxidized to oxygen, and lactic acid was oxidized to oxide (Fig. 10a). In the photocatalytic degradation, oxygen acquires electrons and produces superoxide radicals, which oxidizes RhB to CO_2 and water. RhB was oxidized by the holes into CO_2 and water at the same time (Fig. 10b and S3†). The photocatalysis performance of CdS was improved with the increase of hydrophobicity of the sulfur source.

4 Conclusion

A series of CdS samples were successfully prepared through a low-temperature solvothermal method using thioacetamide, thiourea and thiosemicarbazide as the organic sulfur source. All the samples were mesoporous photocatalysts and the specific surface areas of S-NS, S-TAA, S-TA, and S-TSC were calculated to be 164.2, 99.3, 151.3, and 301.1 $m^2\ g^{-1}$, respectively. The rate of hydrogen evolution of S-TAA was 1.7, 2.0 and 3.8 times that of S-TA, S-TSC and S-NS, respectively. The order of the activity of photocatalytic degradation is S-TAA > S-NS > S-TA > S-TSC. Within 60 min, the degradation efficiency of S-TAA on RhB was close to 99.1%. Increasing the hydrophobic chain of the organic sulfur source not only extended the optical absorption edges to the visible light region, but also reduced the resistance of charge transfer, increasing the rate of surface charge transfer and the lifetime of the photoexcited electrons. This provides a controllable route to improve the photocatalytic performance of CdS.

Author contributions

Qiong Zhu: data curation and writing – original draft preparation. Jinhua Wang: data curation and writing – original draft preparation. Si Cheng: supervision and project administration. Hongquan Fu: formal analysis. Juan Zhang: writing – review & editing. Hejun Gao: funding acquisition, methodology, conceptualization, and supervision. Yunwen Liao: investigation.

Conflicts of interest

There are no conflicts to declare.

Acknowledgements

References

1 T. Huo, G. Ba, Q. Deng, F. Yu, G. Wang, H. Li and W. Hou, *Appl. Catal., B*, 2021, **287**, 119995.

2 G. Zhang, Q. Ji, Z. Wu, G. Wang, H. Liu, J. Qu and J. Li, *Adv. Funct. Mater.*, 2018, **28**, 1706462.

3 Y. Guo, Y. Yang, X. Yin, J. Liu and W. Que, *Sustainable Energy Fuels*, 2020, **4**, 2559–2568.

4 D. Ma, Z. Wang, J.-W. Shi, M. Zhu, H. Yu, Y. Zou, Y. Lv, G. Sun, S. Mao and Y. Cheng, *Chem. Eng. J.*, 2020, **399**, 125785.

5 N. Zhong, M. Chen, Y. Luo, Z. Wang, X. Xin and B. E. Rittmann, *Chem. Eng. J.*, 2019, **355**, 731–739.

6 J. Han, Z. Zhu, N. Li, D. Chen, Q. Xu, H. Li, J. He and J. Lu, *Appl. Catal., B*, 2021, **291**, 120108.

7 Y. Liu, Y. Ma, W. Liu, Y. Shang, A. Zhu, P. Tan, X. Xiong and J. Pan, *J. Colloid Interface Sci.*, 2018, **513**, 222–230.

8 C. Bie, J. Fu, B. Cheng and L. Zhang, *Appl. Surf. Sci.*, 2018, **462**, 606–614.

9 Q. Zhu, Y. Sun, F. Na, J. Wei, S. Xu, Y. Li and F. Guo, *Appl. Catal., B*, 2019, **254**, 541–550.

10 B. Sun, P. Qiu, Z. Liang, Y. Xue, X. Zhang, L. Yang, H. Cui and J. Tian, *Chem. Eng. J.*, 2021, **406**, 127177.

11 Y. Luo, X. Liu, L. Tan, Z. Li, K. W. K. Yeung, Y. Zheng, Z. Cui, Y. Liang, S. Zhu, C. Li, X. Wang and S. Wu, *Chem. Eng. J.*, 2021, **405**, 126730.

12 S. S. Hossain, M. Tarek, T. D. Munusamy, K. M. Rezaul Karim, S. M. Roopan, S. M. Sarkar, C. K. Cheng and M. M. Rahman Khan, *Environ. Res.*, 2020, **188**, 109803.

13 B. Archana, N. Kottam, S. Nayak, K. B. Chandrasekhar and M. B. Sreedhara, *J. Phys. Chem. C*, 2020, **124**, 14485–14495.

14 C. Li, S. Du, H. Wang, S. B. Naghadeh, A. L. Allen, X. Lin, G. Li, Y. Liu, H. Xu, C. He, J. Z. Zhang and P. Fang, *Chem. Eng. J.*, 2019, **378**, 122089.

15 Y. Zhao, Y. Lu, L. Chen, X. Wei, J. Zhu and Y. Zheng, *ACS Appl. Mater. Interfaces*, 2020, **12**, 46073–46083.

16 M. Junaid, M. Imran, M. Ikram, M. Naz, M. Aqeel, H. Afzal, H. Majeed and S. Ali, *Appl. Nanosci.*, 2019, **9**, 1593–1602.

17 J. Wang, Q. Zhu, Y. Liao, H. Fu, J. Chang, Y. Zhang, T. Kan, H. Gao and W. Huang, *J. Alloys Compd.*, 2021, **883**, 160832.

18 Y. Ma, Y. Bian, Y. Liu, A. Zhu, H. Wu, H. Cui, D. Chu and J. Pan, *ACS Sustainable Chem. Eng.*, 2018, **6**, 2552–2562.

19 S. Wang, B. Zhu, M. Liu, L. Zhang, J. Yu and M. Zhou, *Appl. Catal., B*, 2019, **243**, 19–26.

20 Q. Wu, A. B. Abdeta, D.-H. Kuo, H. Zhang, Q. Lu, J. Zhang, O. A. Zelekew, M. T. Mosisa, J. Lin and X. Chen, *J. Mater. Chem. A*, 2022, **10**, 5328–5349.

21 O. A. Zelekew, D.-H. Kuo, J. M. Yassin, K. E. Ahmed and H. Abdullah, *Appl. Surf. Sci.*, 2017, **410**, 454–463.

22 J. Yan, Z. Wei, M. Xu, Z. Jiang and W. Shangguan, *Catalysts*, 2020, **10**, 1478.

23 B. Wang, C. Chen, Y. Jiang, P. Ni, C. Zhang, Y. Yang, Y. Lu and P. Liu, *Chem. Eng. J.*, 2021, **412**, 128690.

24 J. Xu, X. Li, J. Niu, M. Chen and J. Yue, *J. Alloys Compd.*, 2020, **834**, 155061.

25 F. Vaquero, R. M. Navarro and J. L. G. Fierro, *Appl. Catal., B*, 2017, **203**, 753–767.

26 F. Vaquero, R. M. Navarro and J. L. G. Fierro, *Int. J. Hydrogen Energy*, 2016, **41**, 11558–11567.

27 Y. Huang, F. Sun, T. Wu, Q. Wu, Z. Huang, H. Su and Z. Zhang, *J. Solid State Chem.*, 2011, **184**, 644–648.

28 H.-z. Zhang, H. Maimaiti, P.-s. Zhai, S.-X. Wang and B. Xu, *Appl. Surf. Sci.*, 2021, **542**, 148639.

29 J. Zhang, Y. Song, X. Dong, H. Jiang, J. Tang and H. Li, *J. Mater. Sci.*, 2020, **55**, 11167–11176.

30 C.-H. Hsiao, C.-W. Chen, H.-S. Chen, P.-L. Hsieh, Y.-A. Chen and M. H. Huang, *J. Mater. Chem. C*, 2021, **9**, 5992–5997.

31 Y. Zhu, J. Chen, L. Shao, X. Xia, Y. Liu and L. Wang, *Appl. Catal., B*, 2020, **268**, 118744.

32 Y. Zhao, C. Shao, Z. Lin, S. Jiang and S. Song, *Small*, 2020, **16**, 2000944.

33 M. Li, J. Li and Z. Jin, *Dalton Trans.*, 2020, **49**, 5143–5156.

34 H. Lv and H. Sun, *ACS Omega*, 2020, **5**, 11324–11332.

35 R. K. Chava, J. Y. Do and M. Kang, *J. Mater. Chem. A*, 2019, **7**, 13614–13628.

36 Y. Lin, Q. Zhang, Y. Li, Y. Liu, K. Xu, J. Huang, X. Zhou and F. Peng, *ACS Sustainable Chem. Eng.*, 2020, **8**, 4537–4546.

37 X. Chen, H. Sun, D.-H. Kuo, A. B. Abdeta, O. A. Zelekew, Y. Guo, J. Zhang, Z. Yuan and J. Lin, *Appl. Catal., B*, 2021, **287**, 119992.

38 Q. Li, X.-Q. Qiao, Y. Jia, D. Hou and D.-S. Li, *Appl. Surf. Sci.*, 2019, **498**, 143863.

39 J. Guo, Y. Liang, L. Liu, J. Hu, H. Wang, W. An and W. Cui, *Appl. Surf. Sci.*, 2020, **522**, 146356.

40 M. Imran, M. Ikram, A. Shahzadi, S. Dilpazir, H. Khan, I. Shahzadi, S. A. Yousaf, S. Ali, J. Geng and Y. Huang, *RSC Adv.*, 2018, **8**, 18051–18058.

41 J. Wang, S. Yang, J. Chang, S. Pang, H. Fu, F. Jiang, Y. Liao and H. Gao, *J. Electron. Mater.*, 2021, **50**, 2444–2453.

42 Y. Hu, X. Hao, Z. Cui, J. Zhou, S. Chu, Y. Wang and Z. Zou, *Appl. Catal., B*, 2020, **260**, 118131.

43 J. Xu, X. Yan, Y. Qi, Y. Fu, C. Wang and L. Wang, *Chem. Eng. J.*, 2019, **375**, 122053.

44 Z.-W. Zhang, Q.-H. Li, X.-Q. Qiao, D. Hou and D.-S. Li, *Chin. J. Catal.*, 2019, **40**, 371–379.

45 H. Guo, C.-G. Niu, C.-Y. Feng, C. Liang, L. Zhang, X.-J. Wen, Y. Yang, H.-Y. Liu, L. Li and L.-S. Lin, *Chem. Eng. J.*, 2020, **385**, 123919.

46 T.-S. Kang, A. P. Smith, B. E. Taylor and M. F. Durstock, *Nano Lett.*, 2009, **9**, 601–606.

47 X. Ning, J. Li, B. Yang, W. Zhen, Z. Li, B. Tian and G. Lu, *Appl. Catal., B*, 2017, **212**, 129–139.

48 X. Chen, T. Huang, D.-H. Kuo, H. Sun, P. Li, O. A. Zelekew, A. B. Abdeta, Q. Wu, J. Zhang, Z. Yuan and J. Lin, *Appl. Catal., B*, 2021, **298**, 120542.

49 Y. Yang, Q. Meng, X. Jiang, S. Meng, X. Zheng, S. Zhang, X. Fu and S. Chen, *ACS Appl. Energy Mater.*, 2020, **3**, 7736–7745.

50 X. Lu, C. Y. Toe, F. Ji, W. Chen, X. Wen, R. J. Wong, J. Seidel, J. Scott, J. N. Hart and Y. H. Ng, *ACS Appl. Mater. Interfaces*, 2020, **12**, 8324–8332.

51 K. Hareesh, S. D. Dhole, D. M. Phase and J. F. Williams, *Mater. Res. Bull.*, 2019, **110**, 82–89.

52 D. Wang, J. Liu, M. Zhang, Y. Song, Z. Zhang and J. Wang, *Appl. Surf. Sci.*, 2019, **498**, 143843.

53 C. Feng, Z. Chen, J. Jing, M. Sun, H. Tong and J. Hou, *Phys. B*, 2020, **594**, 412363.

54 J. Li, T. Lu, Z. Zhao, R. Xu, Y. Li, Y. Huang, C. Yang, S. Zhang and Y. Tang, *Inorg. Chem. Commun.*, 2020, **121**, 108236.

55 X. Tang, H. Liu, C. Yang, X. Jin, J. Zhong and J. Li, *Colloids Surf., A*, 2020, **599**, 124880.

56 J. Zhang, Z. Zhang, W. Zhu and X. Meng, *Appl. Surf. Sci.*, 2020, **502**, 144275.

57 T. Zhang, X. Wang, Z. Sun, Q. Liang, M. Zhou, S. Xu, Z. Li and D. Sun, *Solid State Sci.*, 2020, **107**, 106350.

58 Y. Lin, D. Pan and H. Luo, *Mater. Sci. Semicond. Process.*, 2021, **121**, 105453.

59 W. Yue, Z. Wang, J. Gong, Z. Wang and Y. Dong, *Mater. Sci. Semicond. Process.*, 2021, **126**, 105671.